

Tidal generation of internal waves from a periodic array of steep ridges

By JONAS NYCANDER

Department of Meteorology, Stockholm University, Stockholm, Sweden

(Received 15 October 2004 and in revised form 24 April 2006)

The generation of internal gravity waves by an oscillatory tidal flow over a periodic array of thin vertical walls is calculated analytically. For small values of the non-dimensional height $B = 2\pi HN/L\omega$, the radiated power per wall is the same as for a single thin wall, and proportional to B^2 , in agreement with the linear scaling. (Here H is the wall height, N the buoyancy frequency, L the wall spacing, and ω the tidal frequency.) The radiated power is periodic in B with period 2π . It diverges logarithmically for $B = (1 + 2n)\pi$, and vanishes for $B = 2n\pi$.

1. Introduction

Mixing in the deep ocean is mainly caused by breaking internal waves. The interaction of tidal currents with rough topography is an important energy source for the internal wave field (Munk & Wunsch 1998; Polzin *et al.* 1997; Ledwell *et al.* 2000), and it is therefore of interest to compute the conversion rate of barotropic tidal energy to internal wave energy.

Several such computations have recently been performed for the global ocean (Arbic *et al.* 2004; Egbert, Ray & Bills 2004; Nycander 2005). They were all based on linear wave theory, employing a linearized boundary condition at the bottom. This approximation requires that the bottom slope is subcritical (Bell 1975*a*), i.e. smaller than ω/N , where ω is the tidal frequency and N the buoyancy frequency. However, Nycander (2005) found that approximately half of the total computed conversion rate occurs at points where the slope is supercritical, and the linear theory therefore invalid. It was also found that insufficient resolution of the bottom topography was the most important source of uncertainty of the computation. When higher resolution data become available, the problem of supercritical slope will become even more serious, since the slope is in general steeper at smaller scales.

The main motivation for the present work is the desire to find the basic scaling of the conversion rate when the slope is supercritical. To do this, one should consider a sequence of different topographies, whose height fields differ only by a multiplicative coefficient H . If H is so small that the bottom slope is subcritical everywhere, we know from linear wave theory that the conversion rate is proportional to H^2 . We seek the scaling for larger values of H .

A simple energy argument indicates that the conversion rate should saturate at supercritical slopes. To see this we first estimate the energy required to displace a fluid parcel along sloping topography. According to linear theory, the vertical displacement of such a parcel during a tidal cycle is of the order $\delta z \sim sU/\omega$, where s is the slope and U the tidal velocity. This corresponds to the potential energy $N^2\delta z^2 \sim U^2(sN/\omega)^2$ per unit mass. Hence, the kinetic energy U^2 due to the tidal motion is insufficient to lift the parcel this distance if $sN/\omega > 1$, i.e. if the slope is supercritical.

In general, the energy conversion rate for supercritical slopes can only be found numerically. Such calculations were performed by Khatiwala (2003) for moderate supercriticality, $sN/\omega < 1.8$. For a truncated sine topography he found that the conversion rate saturates when the slope becomes supercritical, but for a Gaussian ridge he found no saturation.

There are also a few idealized topographies for which an exact solution has been found. These include a thin vertical wall (a ‘knife edge’) (St Laurent *et al.* 2003; Llewellyn Smith & Young 2003), a rectangular ridge of finite width (St. Laurent *et al.* 2003), and a triangular ridge (Petrelis, Llewellyn Smith & Young 2006). In all these cases the conversion at a single ridge was considered, and the depth D of the ocean was considered to be finite. It was found that if the height H of the ridge is less than $D/2$, the conversion rate is approximately within a factor two of the linear result. Hence, the conversion rate is proportional to H^2 even in the supercritical regime in these cases, until H becomes comparable to D (then the conversion increases even more strongly with H).

These results have led some authors to conclude that the conversion rate in general scales as H^2 in the supercritical regime. However, while the bottom slope in the ridge problems mentioned above is supercritical, it can be argued that the main non-dimensional parameter there is in fact H/D , which is not the same as the criticality of the slope. This is most clearly the case for the knife-edge problem. Accordingly, the main physical effect seen in these problems is the flow acceleration over a ridge for finite H/D . Since the flow is incompressible, the mass flux is the same across all vertical sections, and if the ridge occupies a large fraction of the ocean depth the total velocity at the ridge is much larger than the background tidal velocity. (Note that the velocity associated with the wave field is not small compared to the background velocity in these problems.) This flow acceleration explains the increased conversion compared to the linear result, since the linear (i.e. subcritical) scaling implicitly assumes that the tidal velocity at the ridge is the same as far away from the ridge.

The exact solutions mentioned above are appropriate for application to a single and very high ocean ridge, such as the Hawaiian ridge, but not to extended regions of supercritical but moderately high topography. In the latter case, the main physical effect is not flow acceleration, but rather ‘shadowing’. If two neighbouring ridges have supercritical slopes, there is a region in the valley between them from which wave characteristics can only reach the water above after reflection by the ridges; this is the ‘shadow zone’, see figure 1. As H increases, the shadow zone becomes larger, while the vertical extent of the unshadowed region saturates. It is tempting to speculate that this leads to saturation of the conversion rate, too. This idea is supported by the numerical simulations by Khatiwala (2003).

With a single ridge there is no shadow zone. In order to study shadowing, we will instead study a periodic array of thin vertical walls (or knife edges). The ocean depth will be assumed to be infinite, which means that a radiation condition is imposed at some level above the topography to exclude waves with downward group velocity. This is done in order to obtain an analytically solvable problem, but there is also a more fundamental reason for this assumption. The wave energy generated at the topography must be allowed to leave the domain somewhere, since there is no dissipation in the problem. When studying a single ridge, as done by St Laurent *et al.* (2003) and Llewellyn Smith & Young (2003), it is natural to allow the waves to escape horizontally, through the lateral boundaries. If the topography is periodic, on the other hand, this is not possible, and we instead let them escape vertically, through the upper boundary. This approach was used by Bell (1974a) and Balmforth, Ierly & Young (2002).

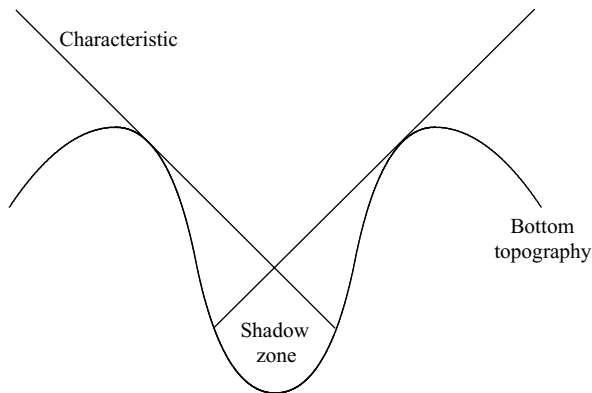


FIGURE 1. Illustration of shadowing. The straight lines are internal wave characteristics that connect to the region above the topography.

Both approaches are approximations compared to the real ocean. With radiation conditions at the lateral boundaries, the reflection from topographic features outside the domain is neglected; with a radiation condition at the upper boundary we neglect the reflection from the sea surface. For the lowest vertical modes it is obviously a bad approximation to neglect reflection from the sea surface. High modes, on the other hand, are much more likely to be decorrelated, or even absorbed, before reaching the topography again after being reflected. (This is a result of refraction by density inhomogeneities, and of nonlinear processes such as wave breaking, cf. Bell 1975*b*.) In this case the coherent interaction between the topography and the waves reflected from the surface can be neglected. High modes are generated by topographic length scales L satisfying $L \ll \overline{ND}/\omega$, where \overline{N} is the vertical average of the buoyancy frequency. In the open ocean, \overline{ND}/ω is typically several tens of kilometres. According to the linear computations by Nycander (2005), most of the conversion in the global ocean is done by topographic scales less than ten kilometres. For such length scales, neglecting reflection from the sea surface should not be a serious problem.

In the problem with a single knife edge and finite depth studied by Llewellyn Smith & Young (2003), the boundary condition at the upper surface effectively imposes a vertical periodicity of the solution, as can be understood from the representation of the Green's function with the help of an infinite series of mirror sources (see § 3 and figure 8 below). The nature of the wave equation to be solved translates the vertical periodicity to horizontal periodicity. In the present problem, with a periodic knife edge and infinite depth, the boundary condition imposes horizontal periodicity, and the wave equation translates this to vertical periodicity. Thus, there is horizontal as well as vertical periodicity in both problems. This geometric similarity means that the two problems are almost identical from a mathematical point of view, and we can rely heavily on the results by Llewellyn Smith & Young (2003) in the calculations. In fact, the conversion rate in the present case can be regarded as a continuation of their result, obtained by formally allowing the ridge height to be larger than the ocean depth.

2. Basic equations

From the linearized hydrostatic fluid equations in the Boussinesq approximation the following equation for internal waves can be derived:

$$\frac{\partial^4 \psi}{\partial z_*^2 \partial t^2} + N^2 \frac{\partial^2 \psi}{\partial x_*^2} = 0. \quad (1)$$

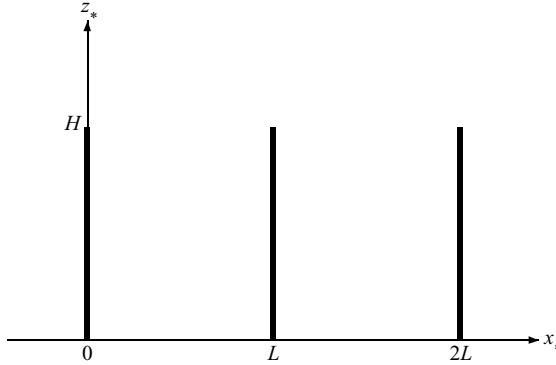


FIGURE 2. The bottom topography, consisting of a periodic series of thin vertical walls, which have height H and are separated by length L .

Here $\psi(x_*, z_*, t)$ is the streamfunction of the wave field (excluding the background tide), so that the velocity is given by $(u, w) = (-\partial\psi/\partial z_*, \partial\psi/\partial x_*)$, and N is the buoyancy frequency, which we assume to be constant. We assume that the bottom topography consists of a periodic series of thin vertical walls (or ridges), see figure 2. The kinematic bottom boundary condition is then

$$\psi = Uz_* \cos(\omega t) \quad \text{on} \quad (x_* = nL, 0 < z_* < H) \quad \text{and on} \quad z_* = 0, \quad (2)$$

where ω is the tidal frequency, H the height of the ridges, L the distance between adjacent ridges, and n any integer.

We consider time-periodic solutions, setting

$$\psi = U \operatorname{Re}\{e^{-i\omega t} \varphi_*\} = U(\varphi_{*r} \cos \omega t + \varphi_{*i} \sin \omega t).$$

Inserting this into (1) and (2) we obtain

$$\frac{\partial^2 \varphi_*}{\partial x_*^2} = \frac{\omega^2}{N^2} \frac{\partial^2 \varphi_*}{\partial z_*^2} \quad (3)$$

and the boundary condition

$$\varphi_* = z_* \quad \text{on} \quad (x_* = nL, 0 < z_* < H) \quad \text{and on} \quad z_* = 0. \quad (4)$$

The energy conversion at one of the ridges (per unit length along the ridge) is given by the following equation (Llewellyn Smith & Young 2003):

$$C = \frac{\rho_0 N^2 U^2}{\omega} \int_0^H z_* \left. \frac{\partial \varphi_{*i}}{\partial x_*} \right|_{x_*=0^+} dz_*. \quad (5)$$

Notice that the Coriolis parameter (i.e. the background rotation) has been neglected for convenience, but can be taken into account simply by replacing ω^2 by $\omega^2 - f^2$ in (3).

We now introduce the following dimensionless variables:

$$x = \frac{2\pi}{L} x_*, \quad z = \frac{2\pi N}{L\omega} z_*, \quad \varphi = \frac{2\pi N}{L\omega} \varphi_*.$$

They are chosen so that the ridge spacing is 2π and the slope of the characteristics is 45° . The final form of the wave equation is then

$$\frac{\partial^2 \varphi}{\partial x^2} = \frac{\partial^2 \varphi}{\partial z^2}, \quad (6)$$

with the boundary condition

$$\varphi = z \quad \text{on} \quad (x = 2\pi n, 0 < z < B) \quad \text{and on} \quad z = 0, \quad (7)$$

where the non-dimensional ridge height is defined by

$$B = 2\pi \frac{HN}{L\omega}. \quad (8)$$

We must also apply a radiation condition at some level above the ridges to exclude waves that have downward group velocity. The energy conversion rate becomes

$$C = \frac{\rho_0 L^2 U^2 \omega^2}{4\pi^2 N} I(B), \quad (9)$$

where $I(B)$ is a non-dimensional function defined by

$$I(B) = \int_0^B z \left. \frac{\partial \varphi_i}{\partial x} \right|_{x=0^+} dz. \quad (10)$$

Notice that the only non-dimensional parameter of the problem is the non-dimensional ridge height B . Since B determines the amount of shadowing, it can also be regarded as a criticality parameter, although the slope at each ridge is of course supercritical regardless of the value of B .

For $I(B) \sim B^2$, (9) reduces to the well-known linear scaling for the conversion, $C_{lin} \sim \rho_0 U^2 H^2 N$ (Bell 1975a). We therefore expect I to be proportional to B^2 in the ‘subcritical’ case, $B \ll 1$. The purpose of the present work is to determine $I(B)$ for arbitrary B .

3. The Green’s function

Following Llewellyn Smith & Young (2003) we introduce the Green’s function $G(x, z, z')$, defined by

$$\frac{\partial^2 G}{\partial x^2} - \frac{\partial^2 G}{\partial z^2} = \sum_{n=-\infty}^{\infty} \delta(x - 2\pi n) \delta(z - z'), \quad (11)$$

by the boundary condition

$$G(x, 0, z') = 0, \quad (12)$$

and by the radiation condition.

The full Green’s function G takes into account a periodic array of sources at $(2\pi n, z')$, and the boundary condition at $z = 0$. We will now construct G step by step, starting with the Green’s function G_1 for a single source on the infinite (x, z) -plane. Assuming without restriction that the source is situated at $(x, z) = (0, 0)$ we have

$$\frac{\partial^2 G_1}{\partial x^2} - \frac{\partial^2 G_1}{\partial z^2} = \delta(x) \delta(z). \quad (13)$$

The radiation condition requires that the group velocity is upward above the source, and downward below the source. In Appendix A it is shown that this leads to

$$\frac{\partial G_1}{\partial z} = \begin{cases} i\mathcal{H} \frac{\partial G_1}{\partial x}, & z > 0 \\ -i\mathcal{H} \frac{\partial G_1}{\partial x}, & z < 0, \end{cases} \quad (14)$$

where \mathcal{H} denotes the Hilbert transform, which is defined in Appendix A.

A particular solution of (13) is most easily found in the rotated coordinate system ξ, η defined by

$$x = \frac{1}{\sqrt{2}}(\xi - \eta), \quad z = \frac{1}{\sqrt{2}}(\xi + \eta).$$

Equation (13) becomes

$$\frac{\partial^2 G_1}{\partial \xi \partial \eta} = -\frac{1}{2} \delta(\xi) \delta(\eta).$$

This can easily be integrated twice, giving the particular solution

$$G_{1p} = -\frac{1}{2} H_s(\xi) H_s(\eta),$$

where H_s is the symmetrized step function:

$$H_s(x) = \begin{cases} \frac{1}{2}, & x > 0 \\ -\frac{1}{2}, & x < 0. \end{cases}$$

Transforming back to the (x, z) -system, we obtain

$$G_{1p} = -\frac{1}{4} \left[\Pi \left(\frac{x}{2z} \right) - \frac{1}{2} \right],$$

where Π is the rectangle function:

$$\Pi(x) = \begin{cases} 1, & |x| < \frac{1}{2} \\ 0, & |x| > \frac{1}{2}. \end{cases}$$

We must then add a homogeneous solution of (13) in order to satisfy the radiation condition. Identifying G_{1p} with the real part of G_1 , we can determine the imaginary part from (14). Using the relation

$$\mathcal{H} \Pi \left(\frac{x}{a} \right) = \frac{1}{\pi} \ln \left| \frac{2x - |a|}{2x + |a|} \right|,$$

we obtain after some calculations

$$G_1 = -\frac{1}{4} \left[\Pi \left(\frac{x}{2z} \right) - \frac{1}{2} \right] + \frac{i}{4\pi} \ln(|x + z||x - z|). \tag{15}$$

This is the Green's function for a single source on an infinite plane. The real part is displayed in figure 3. Notice that the values in the four quadrants (i.e. $1/8, -1/8, 1/8, -1/8$ going clockwise from the x -axis) form a discrete saddle point at the source.

Next, we construct the Green's function $G_2(x, z, z')$ of a single source at $(0, z')$ with a reflecting boundary at $z = 0$. This is easily done by adding a negative mirror source at $(0, -z')$. We obtain

$$\begin{aligned} G_2(x, z, z') &= G_1(x, z, z') - G_1(x, z, -z') \\ &= \frac{1}{4} \left[-\Pi \left(\frac{x}{2(z - z')} \right) + \Pi \left(\frac{x}{2(z + z')} \right) \right] \\ &\quad + \frac{i}{4\pi} \ln \left(\frac{|x + z - z'||x - z + z'|}{|x + z + z'||x - z - z'|} \right). \end{aligned} \tag{16}$$

The real part of G_2 is displayed in figure 4.

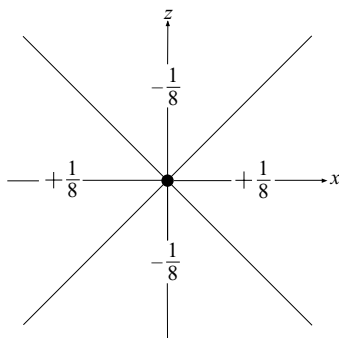


FIGURE 3. The real part of the Green's function G_1 defined in (15), showing the internal wave radiation from a point source (marked by a solid circle) at the origin on an infinite vertical plane.

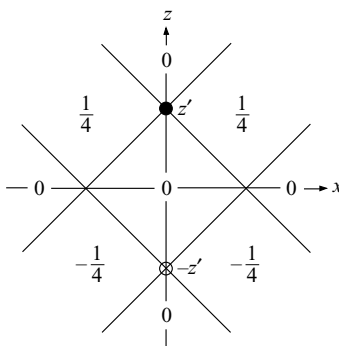


FIGURE 4. The real part of the Green's function $G_2(x, z, z')$ defined in (16), describing the internal wave radiation from a point source at $(0, z')$ with a reflecting surface along the x -axis. Here and in subsequent figures, the solid circles denote sources and the open circles mirror sources, and the region $z < 0$, where the negative mirror sources in figures 4–7 are situated, is not part of the model domain.

Finally, we obtain the full Green's function G as an infinite series of horizontally displaced functions G_2 :

$$G(x, z, z') = \sum_{n=-\infty}^{\infty} G_2(x + 2\pi n, z, z'). \tag{17}$$

The imaginary part,

$$G_i(x, z, z') = \frac{1}{4\pi} \sum_{n=-\infty}^{\infty} \ln \left(\frac{|x + 2\pi n + z - z'| |x + 2\pi n - z + z'|}{|x + 2\pi n + z + z'| |x + 2\pi n - z - z'|} \right),$$

can be rewritten in a simpler form. Summing the terms associated with the characteristics with negative slope separately, using the notation

$$\chi_{\pm} = \frac{1}{2}(x + z \pm z'),$$

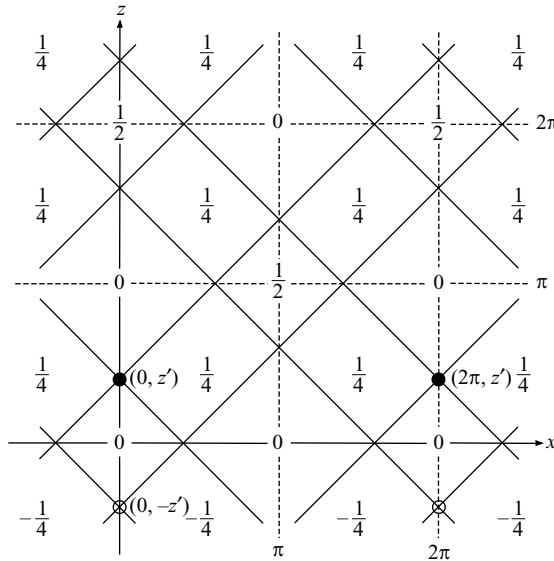


FIGURE 5. The real part of the Green's function $G(x, z, z')$ defined in (17), with sources at $(2\pi n, z')$ and a reflecting surface along the x -axis, for the case $0 < z' < \pi$.

we obtain

$$\begin{aligned} \sum_{n=-\infty}^{\infty} \ln \left| \frac{x+z-z'+2\pi n}{x+z+z'+2\pi n} \right| &= \sum_{n=-\infty}^{\infty} \ln \left| \frac{\chi_- + \pi n}{\chi_+ + \pi n} \right| \\ &= \ln \left| \frac{\chi_-}{\chi_+} \right| + \sum_{n=1}^{\infty} \ln \left| \frac{(\chi_- + \pi n)(\chi_- - \pi n)}{(\chi_+ + \pi n)(\chi_+ - \pi n)} \right|. \end{aligned}$$

The series can be calculated using the following relation, which is equation (1.521.2) in Gradshteyn & Ryzhik (2000):

$$\sum_{n=1}^{\infty} \ln \left(1 - \frac{\chi^2}{n^2 \pi^2} \right) = \ln \sin |\chi| - \ln |\chi|.$$

The result is

$$\sum_{n=-\infty}^{\infty} \ln \left| \frac{x+z-z'+2\pi n}{x+z+z'+2\pi n} \right| = \ln \left| \frac{\sin \frac{1}{2}(x+z-z')}{\sin \frac{1}{2}(x+z+z')} \right|.$$

Proceeding in a similar way with the terms associated with the characteristics with positive slope, we finally obtain

$$G_i(x, z, z') = \frac{1}{4\pi} \ln \left| \frac{\sin \frac{1}{2}(x+z-z') \sin \frac{1}{2}(x-z+z')}{\sin \frac{1}{2}(x+z+z') \sin \frac{1}{2}(x-z-z')} \right|. \tag{18}$$

The real part G_r , on the other hand, does not simplify, and instead of writing the explicit expression we display it graphically in figures 5 and 6 for $0 < z' < \pi$ and $\pi < z' < 2\pi$, respectively. Notice that the values near any source point form a discrete saddle point, while the values near all other intersections between characteristics, e.g. $(\pi, \pi - z')$, form sloping planes.

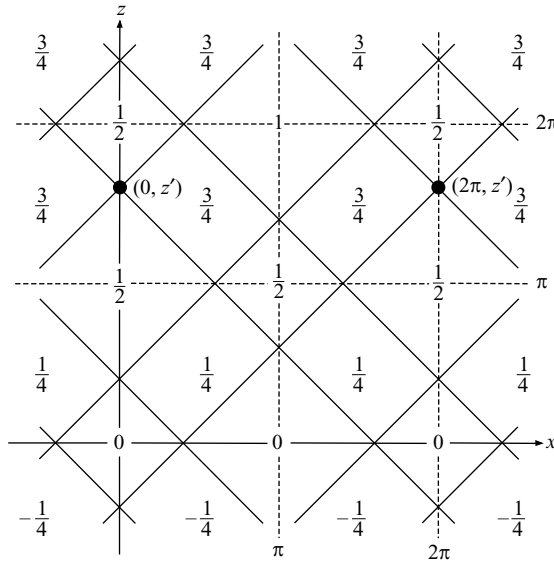


FIGURE 6. The same as figure 5, but for the case $\pi < z' < 2\pi$.

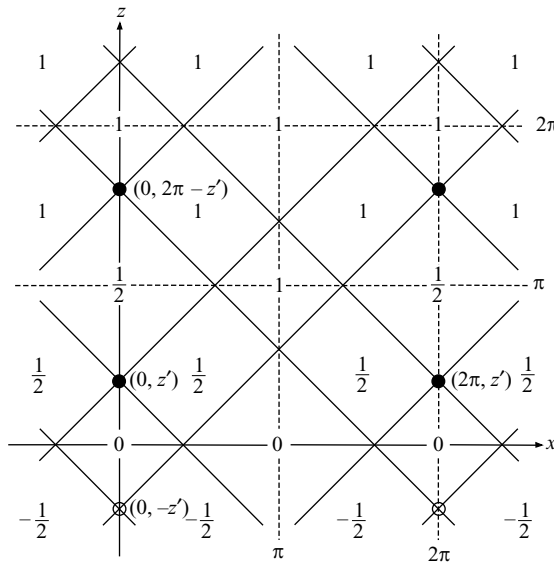


FIGURE 7. The sum $G(x, z, z') + G(x, z, 2\pi - z')$, where $0 < z' < \pi$.

We also consider the sum $G(x, z, z') + G(x, z, 2\pi - z')$. From (18) we find that $G_i(x, z, z') = -G_i(x, z, 2\pi - z')$. The geometric reason for this is that those characteristics that pass through positive sources of $G_i(x, z, z')$ pass through negative mirror sources of $G_i(x, z, 2\pi - z')$. Thus, $G(x, z, z') + G(x, z, 2\pi - z')$ is real. The sum is displayed in figure 7 for $0 < z' < \pi$. Notice that it is constant everywhere in $z > 2\pi - z'$. Thus, two periodic and equal sources at z' and $2\pi - z'$ interact in such a way that no waves are emitted into the region above the sources; the waves are confined to the region near the boundary, as if there were a wave guide.

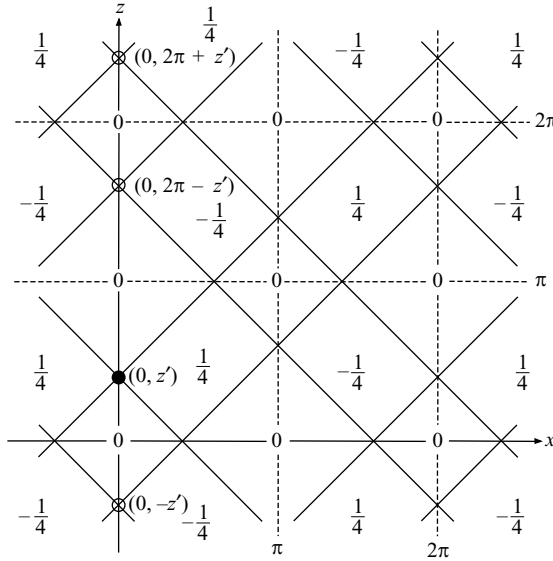


FIGURE 8. The real part of the Green’s function $G_b(x, z, z')$ defined in (19), with a single source at $(0, z')$ and reflecting surfaces along the x -axis and the line $z = \pi$. In this case the model domain is $0 < z < \pi$, and the boundary conditions require an infinite series of vertically displaced mirror sources, alternating between positive and negative sign. This figure corrects figure 3 in Llewellyn Smith & Young (2003), and figure 1 in Robinson (1969).

Finally, we briefly consider the Green’s function G_b for the problem with a single knife edge and an upper boundary at $z = \pi$, considered by Llewellyn Smith & Young (2003). It is obtained as an infinite series of vertically displaced functions G_2 :

$$G_b(x, z, z') = \sum_{n=-\infty}^{\infty} G_2(x, z, z' + 2\pi n). \tag{19}$$

It is easily seen that the imaginary part of G_b is the same as that of G , hence it is also given by (18). The real part, on the other hand, is different, since this is where the sources appear. The real part is displayed in figure 8. This corrects figure 1 in Robinson (1969), which has no sources (i.e. no saddle points), and figure 3 in Llewellyn Smith & Young (2003), which has a source at every intersection between characteristics. The correct figure has one source in the region $0 < z < \pi$.

4. Solution

Using the Green’s function obtained in the previous section, the solution of (6) is represented as

$$\varphi(x, z) = \int_0^B \gamma(z')G(x, z, z') dz', \tag{20}$$

where $\gamma(z)$ can be regarded as a source density along the ridge at $x = 0$. By the construction of the Green’s function, φ automatically satisfies the radiation condition and the boundary condition at $z = 0$, and is periodic in x . It remains to determine $\gamma(z)$ so that the following condition is satisfied:

$$\varphi = z \quad \text{on} \quad (x = 0, 0 < z < B). \tag{21}$$

Inserting (21) into (20) we obtain an integral equation for $\gamma(z)$:

$$z = \int_0^B \gamma(z')G(0, z, z') dz'. \tag{22}$$

The solution procedure depends on the value of B . If $B > \pi$ the characteristics leaving the upper part ($2\pi - B < z < B$) of each wall will intersect the neighbouring wall after being reflected by the bottom. If $B < \pi$ no characteristics will do this.

We begin with the case $B < \pi$. In this case $z' < \pi$, and we see from figure 5 that the real part of $G(0, z, z')$ vanishes over the whole integration interval in (22). Using (18) we obtain

$$z = \frac{i}{2\pi} \int_0^B \gamma(z') \ln \left| \frac{\sin \frac{1}{2}(z - z')}{\sin \frac{1}{2}(z + z')} \right| dz'.$$

This equation has been solved by Llewellyn Smith & Young (2003), with the result

$$\gamma(z) = 2i \sqrt{\frac{1 - \cos z}{\cos z - \cos B}}. \tag{23}$$

The wave field φ is obtained by substituting this equation into (20). Since γ is purely imaginary, only the real part of G affects φ_i . From figure 5 we see that

$$\left. \frac{\partial G_r}{\partial x} \right|_{x=0^+} = \lim_{x \rightarrow 0^+} \frac{1}{4} [\delta(z - z' - x) + \delta(z - z' + x)] = \frac{1}{2} \delta(z - z'). \tag{24}$$

(Notice that the contributions from all the other characteristics cancel each other as $x \rightarrow 0^+$, for $z > 0$.) Differentiating (20) and using (24) we find

$$\left. \frac{\partial \varphi_i}{\partial x} \right|_{x=0^+} = \frac{\gamma_i}{2}.$$

Equation (10) then gives

$$I(B) = \int_0^B z \sqrt{\frac{1 - \cos z}{\cos z - \cos B}} dz. \tag{25}$$

This is the same as (4.6) and (4.7) in Llewellyn Smith & Young if we there set $h = \pi$.

We next consider the case $\pi < B < 2\pi$. In this case we split (20) into two integration intervals, setting

$$\varphi = \varphi_1 + \varphi_2, \tag{26}$$

where

$$\varphi_1(x, z) = \int_0^{2\pi-B} \gamma(z')G(x, z, z') dz', \tag{27}$$

$$\varphi_2(x, z) = \int_{2\pi-B}^B \gamma(z')G(x, z, z') dz'. \tag{28}$$

Guided by the symmetry of the Green's function apparent in figure 7, we assume that the source density over the upper integration interval is symmetric with respect to π , i.e.

$$\gamma(2\pi - z') = \gamma(z'), \quad 2\pi - B < z' < \pi. \tag{29}$$

Over the lower integration interval we assume that the source density is the same as in the previous case $B < \pi$, i.e. that (23) is valid over the interval $0 < z' < 2\pi - B$.

With these assumptions we obtain

$$\varphi_1(0, z) = -\frac{1}{\pi} \int_0^{2\pi-B} \sqrt{\frac{1 - \cos z'}{\cos z' - \cos B}} \ln \left| \frac{\sin \frac{1}{2}(z - z')}{\sin \frac{1}{2}(z + z')} \right| dz'. \tag{30}$$

The integral is calculated in Appendix B, giving

$$\varphi_1(0, z) = \begin{cases} z, & 0 < z < 2\pi - B \\ z - \int_{2\pi-B}^z \sqrt{\frac{1 - \cos z'}{\cos B - \cos z'}} dz', & 2\pi - B < z < B. \end{cases} \tag{31}$$

For the upper integration interval we use the symmetry (29) to write

$$\varphi_2(x, z) = \int_{2\pi-B}^{\pi} \gamma(z') [G(x, z, z') + G(x, z, 2\pi - z')] dz'. \tag{32}$$

From figure 7 we see that

$$G(0, z, z') + G(0, z, 2\pi - z') = \begin{cases} 0, & 0 < z < z' \\ \frac{1}{2}, & z' < z < 2\pi - z' \\ 1, & z > 2\pi - z', \end{cases}$$

where we have assumed $0 < z' < \pi$. Using this, (32) gives

$$\varphi_2(0, z) = \begin{cases} 0, & 0 < z < 2\pi - B \\ \frac{1}{2} \int_{2\pi-B}^z \gamma(z') dz', & 2\pi - B < z < \pi \\ \frac{1}{2} \int_{2\pi-B}^{2\pi-z} \gamma(z') dz' + \int_{2\pi-z}^{\pi} \gamma(z') dz', & \pi < z < B. \end{cases} \tag{33}$$

We see from (31) and (33) that (21) is satisfied on $0 < z < 2\pi - B$ regardless of the source distribution γ on the upper interval. To determine γ on the upper interval we note from (26) that

$$\varphi_2(0, z) = z - \varphi_1(0, z),$$

and insert the known function φ_1 from (31). The resulting equation can easily be solved for γ . The complete source distribution is then given by

$$\gamma(z) = \begin{cases} 2i \sqrt{\frac{1 - \cos z}{\cos z - \cos B}}, & 0 < z < 2\pi - B \\ 2 \sqrt{\frac{1 - \cos z}{\cos B - \cos z}}, & 2\pi - B < z < B. \end{cases} \tag{34}$$

We finally calculate I from (10). Differentiating (27) and using (24) and the fact that $\gamma(z)$ is imaginary in $0 < z < 2\pi - B$ we obtain

$$\left. \frac{\partial \varphi_{1i}}{\partial x} \right|_{x=0^+} = \begin{cases} \frac{1}{2} \gamma_i(z), & 0 < z < 2\pi - B \\ 0, & 2\pi - B < z. \end{cases}$$

Furthermore, from (34) and the symmetry property of G discussed in § 3 we find that the integrand in (32) is real over the whole integration interval. Hence, φ_2 is real, and

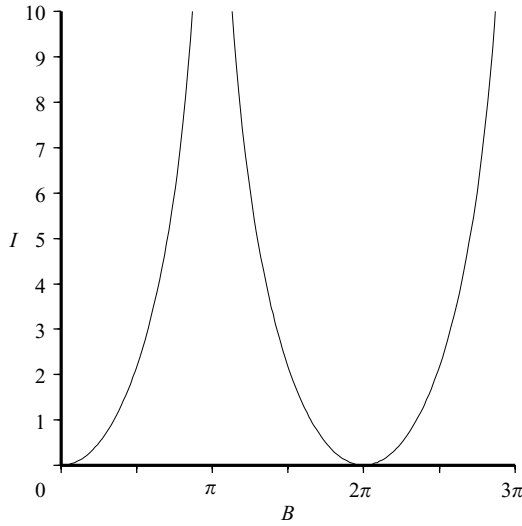


FIGURE 9. Plot of the function $I(B)$ defined in (25) and (36)–(37), showing the radiated power as a function of the dimensionless ridge height B .

does not contribute to (10). We obtain

$$I(B) = \int_0^{2\pi-B} z \sqrt{\frac{1 - \cos z}{\cos z - \cos B}} dz. \tag{35}$$

We may regard this as an extension for $B > \pi$ of (25), using the relation

$$I(2\pi - B) = I(B). \tag{36}$$

For $B > 2\pi$ we have the periodic extension

$$I(B + 2\pi) = I(B). \tag{37}$$

The function $I(B)$ is plotted in figure 9. Notice that $I \sim B^2$ for $B \ll 1$, as expected.

We see from figure 9 that the conversion rate diverges for $B = \pi$, and vanishes for $B = 2\pi$. In order to explain the physical mechanism behind this, the wave field has been calculated explicitly for a few different values of B , cf. Appendix C. The result is shown in figure 10, together with the source density along the walls. The density perturbation has been calculated numerically from (44) and added to a linearly stratified background density field. (The background stratification has been chosen for visual appearance. It is stronger for $B = 0.9\pi$ and $B = 1.1\pi$ than for the other values, since the density perturbation is much larger in these cases.) The contours are isolines of the resulting total density field, the real and imaginary parts showing different time phases of the oscillation.

As shown in figure 10, the source density is largest near the top of the walls. For $B = 0.9\pi$ and $B = 1.1\pi$ we see that the wave generated at one wall top interferes constructively with the wave that is generated at the neighbouring wall top and reflected from the bottom. This leads to enhanced wave radiation. For $B = 1.9\pi$, on the other hand, the wave generated at each wall top interferes destructively with itself after reflection from the bottom and from the neighbouring wall. This leads to weak wave radiation. For $B = 2\pi$ the result is that the wave radiation is completely suppressed, while there is a standing wave between the walls. Also note that the wave

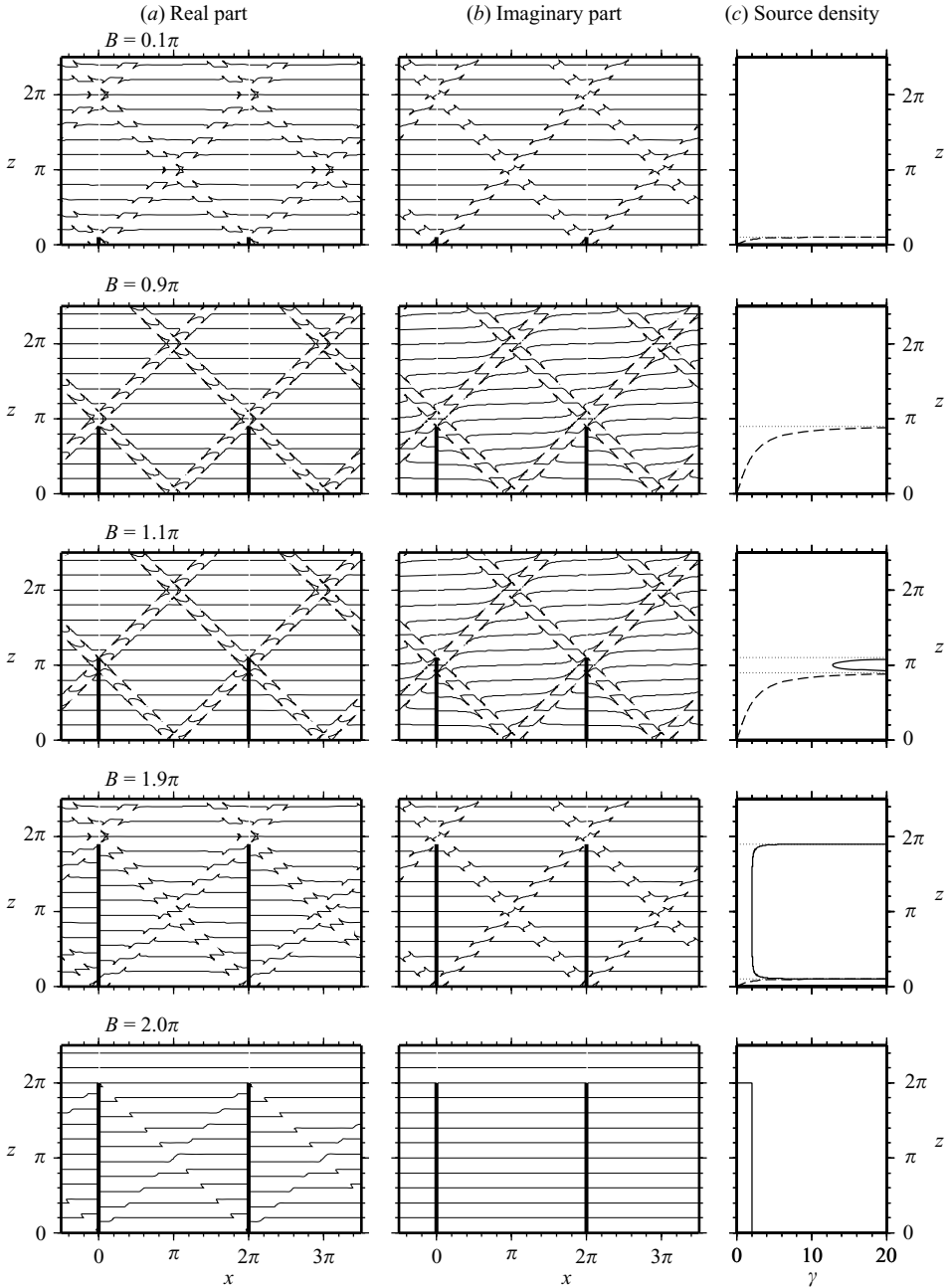


FIGURE 10. Illustration of the wave field and the source density for different values of the dimensionless ridge height B . The contours are curves of constant total density (perturbation plus a linearly stratified background). The real and imaginary parts of the density perturbation has been used in columns (a) and (b), respectively. The source density along the walls is shown in column (c), with the solid curves representing the real part and the dashed curves the imaginary part of γ . The dotted lines denote singularities in the source distribution.

fields for $B = 0.9\pi$ and 1.1π are identical above the topography, and only differ by a standing wave in the region between the walls. The same holds for the wave fields for $B = 0.1\pi$ and 1.9π .

5. Conclusion

The main result of the present work is (25) with the extension (36)–(37), showing how the rate of conversion from barotropic tidal energy to internal wave energy depends on the dimensionless ridge height B of a periodic array of thin and steep ridges. These equations can be converted to dimensional units by using (8) and (9). The dimensionless conversion rate $I(B)$ is displayed in figure 9, while the wave field and source density are shown for a few values of B in figure 10. Note that $I(B)$ is periodic in B .

In the limit $B \ll 1$ it can be shown from (25) that $I \simeq (\pi/4)B^2$, which implies that the conversion at each of the ridges is

$$C \simeq \frac{\pi}{4} \rho_0 U^2 H^2 N.$$

This is the same as the result of Llewellyn Smith & Young (2003) for a single ridge whose height is much smaller than the depth of the ocean. (It is also twice the linear result for the conversion at a ridge with the shape of an Agnesi witch (Bell 1975a)). Thus, in this limit each ridge is an independent source of internal waves.

For larger values of B the ridges interfere with one another. One result of this is the resonance peaks for $B = (1+2n)\pi$, for which the conversion rate diverges. (A different kind of resonance occurs for periodic topography when the ocean depth is finite. In that case the conversion rate given by linear theory diverges if the topographic period coincides with the wavelength of any of the internal modes, cf. Khatiwala 2003.) Another striking result is that the conversion rate vanishes for $B = 2n\pi$; in this case there is only a standing wave between the ridges.

What are the implications of these results for the general scaling of the conversion rate in the supercritical regime? Clearly, they give no support for the idea that I is proportional to B^2 . Perhaps the most basic result is the periodicity of $I(B)$. In an average sense, this may be regarded as saturation for large values of B , although the singularities of $I(B)$ prevent any firm conclusion. In a more realistic case, with non-periodic topography, these singularities would be absent. Presumably, the response curve $I(B)$ for such a topography would be some smoothed version of the curve in figure 9. A small amount of dissipation should have a similar effect.

It was suggested in the introduction that such a saturation should be the result of ‘shadowing’, cf. figure 1. However, we note from the calculations in §4 that the source of the radiated energy is in fact the lowest part of the ridges, for example $0 < z < 2\pi - B$ when $\pi < B < 2\pi$, where the source density is imaginary, cf. figure 10. Thus, ‘shadowing’ gives at best a simplified explanation of the saturation. The real reason lies in a complex interaction between direct wave beams and wave beams reflected by the bottom and the walls.

In conclusion, I believe that the present results support the hypothesis that the conversion rate in general saturates for large values of B , in agreement with the numerical results by Khatiwala (2003). Such a saturation is in contrast to the linear scaling $I(B) \sim B^2$, and would mean that computations based on linear theory, such as those performed by Arbic *et al.* (2004), Egbert *et al.* (2004) and Nycander (2005), overestimate the conversion rate where the slope is supercritical. However, more research is needed to fully confirm this hypothesis.

Most of this work was done while I was participating in the Geophysical Fluid Dynamics Program at Woods Hole Oceanographic Institution during the summer of 2004. I am grateful to Stefan Llewellyn Smith for discussions.

Appendix A. Radiation condition for internal waves

We start from (1) for internal waves. After Fourier transformation it gives the dispersion relation

$$\omega^2 m^2 = N^2 k^2, \quad (\text{A } 1)$$

where (k, m) is the wave vector in Fourier space. We may without restriction take ω to be positive, so that the sign of the vertical phase velocity ω/m is determined by the sign of m . Above the source, the radiation condition requires that the vertical component of the group velocity be positive. From the dispersion relation it may easily be shown that the group velocity and the phase velocity have opposite signs, and the radiation condition can therefore be written

$$m = -\frac{N}{\omega}|k|.$$

Using the dimensionless variables defined in §2, we have

$$m = -|k|. \quad (\text{A } 2)$$

We will now perform an inverse Fourier transformation of this expression. We need the Hilbert transform, defined by

$$\mathcal{H} f(x) = \frac{1}{\pi} \mathcal{P} \int_{-\infty}^{\infty} \frac{f(y)}{y-x} dy,$$

where \mathcal{P} denotes the principle value. The following property of the Hilbert transform can easily be derived. If two functions $g(x)$ and $h(x)$ are related by

$$g = \mathcal{H} \frac{\partial h}{\partial x},$$

then their respective Fourier transforms satisfy

$$\tilde{g} = -|k|\tilde{h},$$

where the Fourier transform is defined by

$$\tilde{g}(k) = \int_{-\infty}^{\infty} e^{-ikx} g(x) dx.$$

From (A 2) we have

$$im\tilde{\varphi} = -i|k|\tilde{\varphi}.$$

After inverse Fourier transformation in z , which is trivial, and in x , which can be done using the above property of the Hilbert transform, we obtain

$$\frac{\partial \varphi}{\partial z} = i\mathcal{H} \frac{\partial \varphi}{\partial x},$$

i.e. the first case in (14).

Below the source the group velocity should be negative, which reverses the sign in (A 2). Proceeding as above, we obtain the second case in (14).

Appendix B. Calculation of integral

To calculate the integral in (30), first differentiate with respect to z :

$$\left. \frac{\partial \varphi_1}{\partial z} \right|_{x=0} = \frac{1}{\pi} \mathcal{P} \int_0^{2\pi-B} \sqrt{\frac{1 - \cos z'}{\cos z' - \cos B}} \frac{\sin z'}{\cos z - \cos z'} dz', \quad (\text{B } 1)$$

where \mathcal{P} denotes the principal part. (The integral in (30) is absolutely convergent at the singularity $z' = z$, while the integral in (B 1) is not. By taking the principal part, equality still holds.) Making the substitution $\cos z' = \xi$, we obtain

$$\frac{\partial \varphi_1}{\partial z} \Big|_{x=0} = \frac{1}{\pi} \mathcal{P} \int_{\cos B}^1 \sqrt{\frac{1-\xi}{\xi-\cos B}} \frac{d\xi}{\cos z - \xi}.$$

Further substituting

$$\sqrt{\frac{\xi - \cos B}{1 - \xi}} = \eta,$$

we obtain

$$\frac{\partial \varphi_1}{\partial z} \Big|_{x=0} = \frac{2}{\pi} \frac{1 - \cos B}{\cos z - 1} \mathcal{P} \int_0^\infty \frac{1}{\eta^2 + \frac{\cos z - \cos B}{\cos z - 1}} \frac{d\eta}{\eta^2 + 1}. \tag{B 2}$$

If $\cos z > \cos B$ there is a singularity for some positive value of η . The integral can then be calculated using the relation

$$\mathcal{P} \int_0^\infty \frac{dx}{(x^2 + a^2)(x^2 - b^2)} = -\frac{\pi}{2a(a^2 + b^2)},$$

which can be derived by the method of residues. We obtain

$$\frac{\partial \varphi_1}{\partial z} \Big|_{x=0} = 1. \tag{B 3}$$

If $\cos z < \cos B$ there is no singularity in the integral (B 2), and we use

$$\mathcal{P} \int_0^\infty \frac{dx}{(x^2 + a^2)(x^2 + b^2)} = \frac{\pi}{2ab(a + b)},$$

which gives

$$\begin{aligned} \frac{\partial \varphi_1}{\partial z} \Big|_{x=0} &= \frac{\cos B - 1}{\cos B - \cos z + \sqrt{(1 - \cos z)(\cos B - \cos z)}} \\ &= 1 - \sqrt{\frac{1 - \cos z}{\cos B - \cos z}}. \end{aligned} \tag{B 4}$$

By integration of (B 3) and (B 4) we finally obtain (31).

Appendix C. Explicit calculation of the density field

For a harmonic internal wave the density perturbation is proportional to the vertical velocity, and therefore to $\partial\varphi/\partial x$. From (20) we obtain

$$\frac{\partial \varphi(x, z)}{\partial x} = \int_0^B \gamma(z') \frac{\partial}{\partial x} G(x, z, z') dz'.$$

Inserting the real part G_r from (17) and the imaginary part G_i from (18) this can be rewritten as

$$\begin{aligned} \frac{\partial \varphi(x, z)}{\partial x} &= \frac{1}{4} \sum_n \text{sign}(x + 2\pi n) [\gamma(x + z + 2\pi n) \\ &\quad + \gamma(-x + z - 2\pi n) - \gamma(-x - z - 2\pi n) - \gamma(x - z + 2\pi n)] \end{aligned}$$

$$\begin{aligned}
& + \frac{i}{8\pi} \int_0^B \gamma(z') \left[\cot\left(\frac{x+z-z'}{2}\right) + \cot\left(\frac{x-z+z'}{2}\right) \right. \\
& \left. - \cot\left(\frac{x+z+z'}{2}\right) - \cot\left(\frac{x-z-z'}{2}\right) \right] dz', \quad (\text{C } 1)
\end{aligned}$$

where each of the four first terms is summed over all n for which the argument of γ is between 0 and B . (Equivalently, we can define γ to be zero outside this interval, and sum over all n .) The integral is evaluated by numerical quadrature.

REFERENCES

- ARBIC, B. K., GARNER, S. T., HALLBERG, R. W. & SIMMONS, H. L. 2004 The accuracy of surface elevations in forward global barotropic and baroclinic tide models. *Deep-Sea Res. II* **51**, 3069–3101.
- BALMFORTH, N. J., IERLY, G. R. & YOUNG, W. R. 2002 Tidal conversion by subcritical topography. *J. Phys. Oceanogr.* **32**, 2900–2914.
- BELL, T. H. 1975*a* Lee waves in stratified flows with simple harmonic time dependence. *J. Fluid Mech.* **67**, 705–722.
- BELL, T. H. 1975*b* Topographically generated internal waves in the open ocean. *J. Geophys. Res.* **80**, 320–327.
- EGBERT, G. D., RAY, R. D. & BILLS, B. G. 2004 Numerical modeling of the global semidiurnal tide in the present day and in the last glacial maximum. *J. Geophys. Res.* **109**, C03003, doi:10.1029/2003JC001973.
- GRADSHTEYN, I. S. & RYZHIK, L. M. 2000 *Table of Integrals, Series, and Products*, 6th edn. Academic.
- KHATIWALA, S. 2003 Generation of internal tides in an ocean of finite depth: analytical and numerical calculations. *Deep-Sea Res. I* **50**, 3–21.
- LEDWELL, J. R., MONTGOMERY, E. T., POLZIN, K. L., ST LAURENT, L. C., SCHMITT, R. W. & TOOLE, J. M. 2000 Evidence for enhanced mixing over rough topography in the abyssal ocean. *Nature* **403**, 179–182.
- LLEWELLYN SMITH, S. G. & YOUNG, W. R. 2003 Tidal conversion at a very steep ridge. *J. Fluid Mech.* **495**, 175–191.
- MUNK, W. H. & WUNSCH, C. I. 1998 Abyssal recipes. II: Energetics of tidal and wind mixing. *Deep-Sea Res. I* **45**, 1977–2010.
- NYCANDER, J. 2005 Generation of internal waves in the deep ocean by tides. *J. Geophys. Res.* **110**, C10028, doi:10.1029/2004JC002487.
- PETRELIS, F., LLEWELLYN SMITH, S. G. & YOUNG, W. R. 2006 Tidal conversion at a submarine ridge. *J. Phys. Oceanogr.* **36**, 1053–1071.
- POLZIN, K. L., TOOLE, J. M., LEDWELL, J. R. & SCHMITT, R. W. 1997 Spatial variability of turbulent mixing in the abyssal ocean. *Science* **276**, 93–96.
- ROBINSON, R. M. 1969 The effects of a barrier on internal waves. *Deep-Sea Res.* **16**, 421–429.
- ST LAURENT, L., STRINGER, S., GARRETT, C. & PERRAULT-JONCAS, D. 2003 The generation of internal tides at abrupt topography. *Deep-Sea Res. I* **50**, 987–1003.